Precambrian Research 324 (2019) 18–31

Contents lists available at ScienceDirect

Precambrian Research

journal homepage: www.elsevier.com/locate/precamres

Revisiting the Precambrian evolution of the Southwestern Tarim terrane: Implications for its role in Precambrian supercontinents

Chuan-Lin Zhang[a,*], Xian-Tao Ye[a], R.E. Ernst[b,c], Yan Zhong[d], Jian Zhang[d], Huai-Kun Li[d], Xiao-Ping Long[e]

[a] College of Oceanography, Hohai University, Nanjing 210093, PR China
[b] Dept. of Earth Sciences, Carleton U., 1125 Colonel By Drive, Ottawa K1S 5B6, Canada
[c] Faculty of Geology and Geography, Tomsk State University, 36 Lenin Ave, Tomsk 634050, Russia
[d] Tianjin Centre, Chinese Geology Survey, Tianjin 100083, PR China
[e] Department of Geology, Northwest University, Xian 710069, PR China

ARTICLE INFO

Keywords:
Southern Tarim terrane
Precambrian evolution
Columbia breakup
Rodinia assembly

ABSTRACT

The Tarim block in NW China consists of a Precambrian basement and late Neoproterozoic to Paleozoic cover sequences. In order to better understand its roles in Precambrian supercontinent evolution, we used SHRIMP and LA-ICPMS U-Pb methods to date late Paleoproterozoic rifting-related mafic dykes and Mesoproterozoic igneous activity in the Precambrian of the southwestern Tarim terrane (STT): 1) WNW trending mafic dyke swarm emplaced at ca. 1785 Ma; 2) Mesoproterozoic bimodal volcanic sequence (the lower member) and marble-clastic-quartzite sequences (the upper member) deposited at ca. 1525 Ma and 1500–1400 Ma, respectively; 3) late Mesoproterozoic granodiorite-augen granite-leucogranite complex emplaced at ca. 1117 Ma. Geochemistry revealed that the 1784 ± 12 Ma mafic dykes were derived from an E-MORB – like mantle source suggesting an extensional setting, and likely linked with coeval major large igneous provinces (LIPs) on several crustal blocks which collectively suggest a pulse of rifting associated with assembly of the Columbia supercontinent. The obtained U-Pb age of 1525 ± 4 Ma from a meta-rhyolite in the bimodal sequence matches a recently discovered 1525–1529 Ma Large Igneous Province from the southern West African craton (Essakane-Sambaraboungou swarm) and formerly adjacent Amazonian craton (Kayser event). Geochemistry of the ca. 1117 Ma granitic intrusions defines their A-type signature. These may be linked to coeval intraplate mafic magmatism of a reconstructed 1110 Ma LIP involving Kalahari, Congo, India (Bundelkhand block), Amazonia cratons. In line with these three newly recognized pulses of Precambrian igneous activities in STT and the significant diachroneity of the Precambrian tectono-magnetic events between the STT and the Northern Tarim terrane (NTT), we argue that the Precambrian basement of the Tarim were most likely composed of two distinct terranes (i.e., the STT and the NTT). These originated from different Precambrian nuclei and they did not amalgamate as the Tarim block until to the early middle Neoproterozoic.

1. Introduction

Precambrian continents amalgamated at 2.1–1.8 Ga and 1.3–0.9 Ga leading to the formation of the Columbia (or Nuna) and Rodinia supercontinents, respectively (Rogers and Santosh, 2002; Zhao et al., 2002, 2011; Li et al., 2008 and references therein). The process from Columbia breakup to Rodinia assembly remains actively researched (Li et al., 2008; Zhang et al., 2012a; Cawood et al., 2013). Despite consensus on the evolution of the main continents (such as Laurentia, Siberia, Australia, India, Congo, Africa and eastern Antarctica), the coupling relationship between some Precambrian continents at the fringe of the supercontinents and the overall evolution of the Precambrian supercontinents remains unclear. These continents at the fringe of the Precambrian supercontinents could play a key role in understanding the evolution from the assembly and breakup of Columbia to the assembly of Rodinia (Li et al., 2008, 2009; Cawood et al., 2016; Zheng et al., 2013; Zilio et al., 2018).

In the past decade, Precambrian studies on the Tarim block in NW China suggested that it was most probably located at the northern fringe of the supercontinent Rodinia (Zhan et al., 2007; Zhao et al., 2012; Zheng et al., 2013; Zhang et al., 2012b, 2013). According to a proposed Neoproterozoic suture zone along the central Tarim and the

* Corresponding author.
E-mail address: zhangchuanlin@hhu.edu.cn (C.-L. Zhang).

https://doi.org/10.1016/j.precamres.2019.01.018
Received 11 September 2018; Received in revised form 14 December 2018; Accepted 29 January 2019
Available online 30 January 2019
0301-9268/

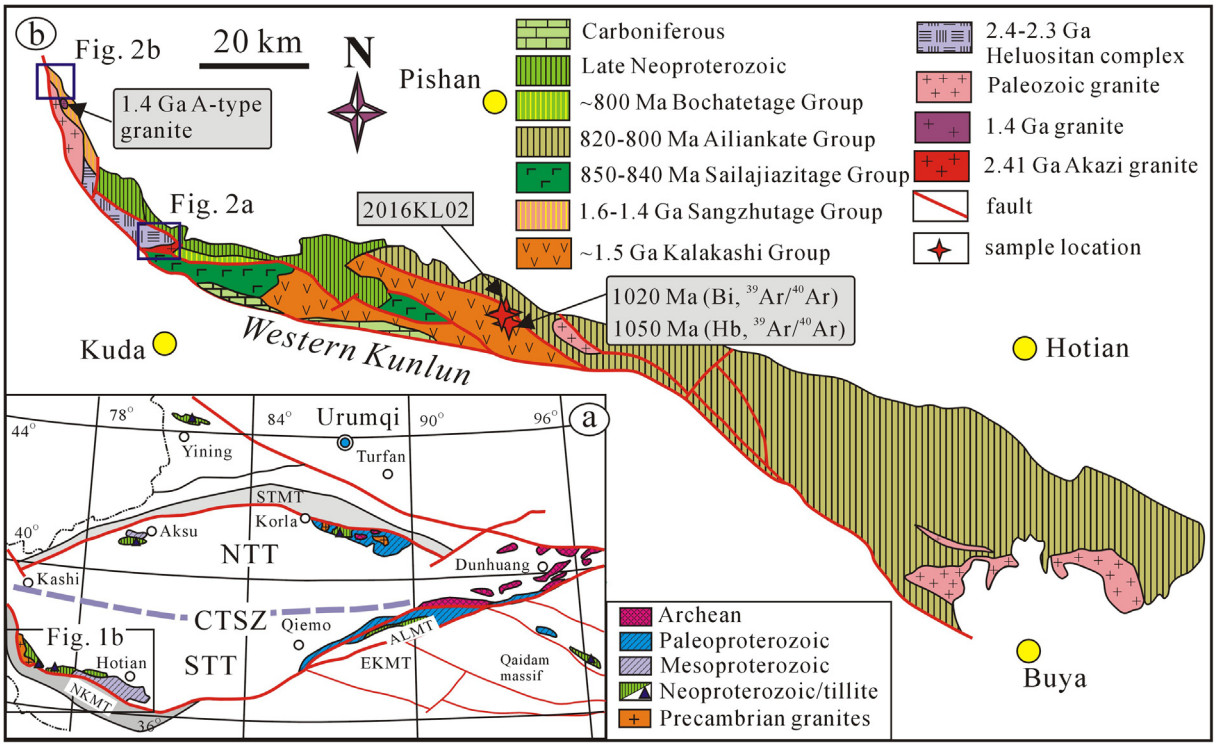

Fig. 1. (a) Tectonic framework of the Tarim Block and its adjacent areas showing the Precambrian terranes along its margin. (b) Main Precambrian units in the southwestern section of the Tarim Block. Hornblende and biotite $^{39}Ar/^{40}Ar$ plateau ages are marked for the high greenschist to amphibolite facies metamorphic Mesoproterozoic Kalakashi Group (modified after Xinjiang BGMR, 1993; Zhang et al., 2003). The Neoproterozoic sequences can be divided into main three members, i.e., member 1, the Sailajiazitage group; member 2, the Ailiankate Group and member 3, the Silu Group (SLG) and Qiakemakelieke Group (QG). Both member 1 and member 2 underwent low greenschist-facies metamorphism and intensive deformation while member 3 exhibits no deformation or metamorphism. NTT-north Tarim terrane, STT-south Tarim terrane, CTSZ-central Tarim suture zone (820–800 Ma, Yin and Nie, 1996; Xu et al., 2013a), STMT-south Tianshan mount, NKMT- north Kunlun mount, ALMT-Altyn mount, EKMT-east Kunlun mount.

presence of late Neoproterozoic blueschist-granulite facies metamorphism along the northern margin of the Tarim block, most geologists have suggested that the two distinct terranes, i.e., the northern Tarim terrane (NTT) and the southern Tarim terrane (STT) (Fig. 1a, Liou et al., 1996; Yin and Nie, 1996; Wu et al., 2012; Xu et al., 2013a; Zuza and Yin, 2017), docked to the northern margin of Australia during 1.0–0.8 Ga and that subduction along the northern Australian margin lasted till to ~740 Ma (Fig. 1a, Zhang et al., 2012b, 2016; Xu et al., 2005, 2009, Xu et al., 2013a,b). On the other hand, in line with the diachroneity of the late Paleoproterozoic metamorphism and distinct continental growth between the NTT and STT, some scholars have suggested that these two basement terranes of the Tarim amalgamated in early to middle Neoproterozoic during the assembly of the Rodinia supercontinent (Guo et al., 2005; Xu et al., 2013a; Zhang et al., 2014a,b; Wu et al., 2018; Yang et al., 2018). In order to address the cause of diachroneity of the late Paleoproterozoic and the early to middle Neoproterozoic metamorphism in different terranes of the Tarim, and to construct a more detailed Precambrian evolution of the Tarim, in this contribution, field observations, petrographic features and zircon/baddeleyite U-Pb ages, in combination with elemental and Sr-Nd-Hf isotopic geochemistry, are used to identify and characterize magmatic pulses during this late Paleoproterozoic to middle Neoproterozoic period, discuss their petrogenesis and to decipher a more detailed Precambrian evolution process of the STT and its setting within supercontinents Columbia and Rodinia. For instance, dating and geochemistry of these magmatic events can potentially matched with coeval magmatic events on other crustal blocks to identify the reconstruction setting for the STT terrane of the Tarim craton within Columbia and Rodinia supercontinents.

2. Regional geology

The Tarim Block shows a typical double-layered structure sequence consisting of a Precambrian basement (pre-Nanhuanian) and a Nanhuanian to Cambrian cover (Lu, 1992, 2008; Xinjiang BGMR, 1993; Feng et al., 1995; Gao and Chen, 2003; Wang et al., 2004). The Precambrian rocks in the Tarim Block are mostly exposed along the northern, eastern and southwestern margins. In central Tarim, Precambrian igneous and metamorphic rocks were also identified in drill core (Fig. 1a) (Li et al., 2003, 2005; Guo et al., 2005; Xu et al., 2013a; Yang et al., 2018).

The major Precambrian rock series of the southwestern Tarim terrane (STT) are mainly composed of the Paleoproterozoic Heluositan complex (ca. 2.40–2.32 Ga) and the ca. 2.41 Ga Akazi pluton (Zhang et al., 2007; Wang et al., 2014; Ye et al., 2016) (Fig. 1b), the Mesoproterozoic greenschist- to amphibolite- facies metamorphosed and intensively folded sedimentary sequences, the greenschist-facies metamorphosed and folded Neoproterozoic volcanic-sedimentary sequences and the Nanhuaian clastic-tillite-carbonate sequences lacking significant metamorphism and deformation (Lu et al., 2008; Zhang et al., 2010, 2016) (Fig. 1b). The Heluositan Complex mainly consists of gneissic granites, orthogneisses and migmatites which underwent ca. 1.9 Ga amphibolite to granulite facies metamorphism (Zhang et al., 2007; Wang et al., 2014; Ye et al., 2016). The Kalakashi Group (KG), composed of almost equal volumes of volcanic rocks and low-maturity clastic rocks, underwent amphibolite-facies metamorphism and strong deformation. This metamorphism is most reliably dated as late Mesoproterozoic on the basis of ca. 1.0 Ga hornblende and biotite $^{39}Ar/^{40}Ar$ plateau ages (Fig. 1b) (Zhang et al., 2003). The metamorphic ages of the KG were suggested to be related to the assemblage of the STT into the Rodinia supercontinent (Zhang et al., 2003). However, the

emplacement age of the KG was poorly known prior to this study. Another Mesoproterozoic member, locally termed the Sangzhutage Group (SZG), is mainly composed of marble and a greenschist-facies metamorphic clastic sequence with minor quartzite. This member was most likely deposited during 1.5–1.4 Ga according to detrital zircon U-Pb ages and the ~1.4 Ga gneissic granites intruding it (Ye et al., 2016; this study). Neoproterozoic units include the greenschist-facies metamorphic Sailajiazitage Group (SG) and the Ailiankate Group (AG). The ca. 850–840 Ma SG volcanic-sedimentary sequence was deposited in a backarc basin while the ca. 800 Ma AG was deposited in a foreland basin caused by southward subduction along the central Tarim (Xu et al., 2013a; Zhang et al., 2016). The Nanhuaian Cambrian-aged cover sequences in STT unconformably overlie the Pre-Nanhuaian sequences. The sedimentary features, rock packages and deposition ages of the Neoproterozoic sequences in the STT were detailed in Zhang et al. (2016).

3. Field observations and petrography

The newly identified mafic dykes and granodiorite-augen granite-leucogranite complexes outcrop in the eastern section of the Heluositan complex and northwestern end of STT, respectively (Fig. 1b; Fig. 2a, b). The orientations of those dykes are relatively coherent, varying from 310° to 330° in strike, and from 70° to 80° in dip to the SW (Fig. 2a). The widths of the dykes are mostly between 2 and 5 m, with some more than 10 m wide. They extend in length at least 300 m to more than 2000 m. At one dyke outcrop of ca. 10 m in width, from fringe to the centre, the rock types gradually change from dolerite through gabbroic dolerite and then to gabbro in the centre (Fig. 3a, b). The chilled contact between the mafic dykes and the gneiss was observed (Fig. 3a).

The mafic dykes in the Heluositan complex are relatively fresh. The diabase consists mainly of clinopyroxene (35–45%), sericitized plagioclase (45–55%), Ti-Fe oxides (5–10%), and minor brown hornblende and biotite (less than 5%). They have typical diabasic textures with xenomorphic mafic minerals and Ti-Fe oxides filling in the spaces between the semi-euhedral bladed plagioclase. Gabbroic diabase is relatively coarse-grained and has similar mineral compositions to the fine-grained diabase. The gabbroic rocks have hypidiomorphic texture. Primary minerals include 40–50% (molar) clinopyroxene (mostly altered to hornblende and actinolite), 40–50% plagioclase, 5–10% Fe–Ti oxides and minor olivine and orthopyroxene (less than 5%, Fig. 3f, g).

The granodiorite- augen granite- leucogranite bodies are emplaced in the SZG (Fig. 2b). These diverse “granitic” rock types intermingle with each other at outcrops and they underwent post-emplacement deformation (Fig. 3c-e), showing consistent gneissic structures with those of the wall rocks. The phenocrysts (augens) in the granite are microcline/orthoclase and their size is typically up to 2 cm to 5 cm, but with some as large as 8–10 cm; these phenocrysts account for about 30–40% of the whole rock (Fig. 3c). The matrix is mainly composed of biotite (1–5%), sericite (5–10%), (quartz (25–35%), orthoclase (20–25%), microcline (15–25%) and minor Ti-Fe oxide (generally less than 1%) (Fig. 3h). Accessory minerals include zircon, apatite and monazite. The granodiorite and the leucogranite are coarse-grained. The granodiorite is mainly composed of biotite (15–25%), plagioclase (30–40%), microcline (10–15%) and quartz (15–25%) while the leucogranite, by orthoclase (30–40%), albite (20–30%) and quartz (20–30%) (Fig. 3i). Subgranulation is commonly seen in the leucogranite possibly due to post-emplacement deformation (Fig. 3i).

4. Analytical methods

Six geochronological samples were analyzed in this study. One gabbro sample (2015D025, 37°05′36″N, 76°57′14″E) was collected from a ~10 m wide mafic dyke in the Heluositan complex, one metarhyolite sample (2016KL02, 37°01′50″N, 78°01′36″E) is from the bimodal volcanic sequence of KG, one sample of feldspar quartz sandstone from the SZG (2016XJ-15, 38°4′27″, 76°06′41″E) and three samples are from the augen granite, granodiorite and leucogranite, respectively (2015KL72, 38°03′43″N, 76°03′48″E; 2016KL10, 38°03′43″N, 76°03′48″E; 2016KL11, 38°03′37″N, 76°03′45″E). Mineral separation was carried out first using conventional magnetic and density techniques to concentrate the non-magnetic heavy fractions. Zircon grains were then extracted by hand-picking under a binocular microscope. Three samples (2016KL02, 2016KL10, 2016KL11) were analyzed using the SHRIMP U–Pb method in the Beijing SHRIMP Centre, Chinese Academy of Geological Sciences. The zircon analytical procedures followed the procedure described by Nelson (1997). U–Th–Pb ratios were determined relative to the TEMROA standard zircon (Black et al., 2004), and the U and Th absolute abundances relative to the SL13 standard zircon. Measured compositions were corrected for common Pb using non-radiogenic ^{204}Pb, and an average crustal composition (Cumming and Richards, 1975) appropriate to the age of the mineral was assumed. Software SQUID 1.0 and ISOPLOT (Ludwig, 2003) were used for data processing. Individual corrected ratios and ages are reported with 1σ analytical errors. The weighted mean ages are quoted at a 95% confidence level. The baddeleyite sample (2015D025), the detrital zircon sample from SZG (2016XJ-15) and zircon sample from the augen granite sample (2015KL72) were analyzed using the LA-ICP-MS method at Tianjing Institute of Geology and Mineral Resources. Instrumental setting and detailed zircon analytical procedure have been described by Hou et al. (2009). 91500, and the GJ-1 zircon standard and Palaborwa baddeleyite standard (2059.8 ± 0.8 Ma) were used to monitor the analyzing zircon and baddeleyite samples, respectively. The concordia and relative probability diagrams are plotted using Isoplot 3, and data are presented with 1σ errors and 95% confidence limits (Ludwig, 2008). All the age data are presented in the Supplementary Table 1 and representative CL images of the dated samples are presented in the Supplementary Fig. 1.

Baddeleyite and zircon Hf isotope analyses were carried out using a New Wave-193 nm ArF-excimer laser-ablation system linked to a Neptune multiple-collector inductively coupled plasma mass spectrometer (LA-MC-ICP-MS) in Tianjin Institute of Geology and Mineral Resources. The analytical results are presented in Supplementary Table 2 and the detailed analytical procedures as well as the related references are listed as footnotes in this table.

Whole-rock major and trace element compositions were analyzed at Guiyang Institute of Geochemistry, Chinese Academy of Sciences. Major elements were analyzed using a Rigaku ZSX100e XRF following the analytical procedures described by Li et al. (2004). Analytical precision is generally better than 2%. Trace elements were analyzed using a Perkin-Elmer Sciex ELAN 6000 ICP-MS following procedures described by Li et al. (2004). Whole-rock compositions are listed in Supplementary Table 3.

Sr-Nd isotopes were determined using a Micromass Isoprobe Multi-collector ICPMS (MC-ICPMS) at Tianjin Institute of Geology and Mineral Resources, Chinese Geology Survey, following the procedure described by Li et al. (2004). Measured ^{87}Sr/^{86}Sr and ^{143}Nd/^{144}Nd ratios were normalized to ^{86}Sr/^{88}Sr = 0.1194 and ^{146}Nd/^{144}Nd = 0.7219, respectively. The reported ^{87}Sr/^{86}Sr and ^{143}Nd/^{144}Nd ratios were respectively adjusted to the NBS SRM 987 standard ^{87}Sr/^{86}Sr = 0.71025 and the Shin Etsu JNdi-1 standard ^{143}Nd/^{144}Nd = 0.512115. Sr-Nd isotope results are listed in Supplementary Table 4.

5. Analytical results

5.1. Baddeleyite/zircon U-Pb ages

5.1.1. Baddeleyite U-Pb age of the mafic dyke in yecheng

The baddeleyite grains are pinkish, tabular in form and 50–70 μm in size. They show deep color in CL images and at the rim of some grains, the baddeleyite was replaced by zircon possibly due to post-emplacement hydrothermal alteration. As only about 30 grains were obtained

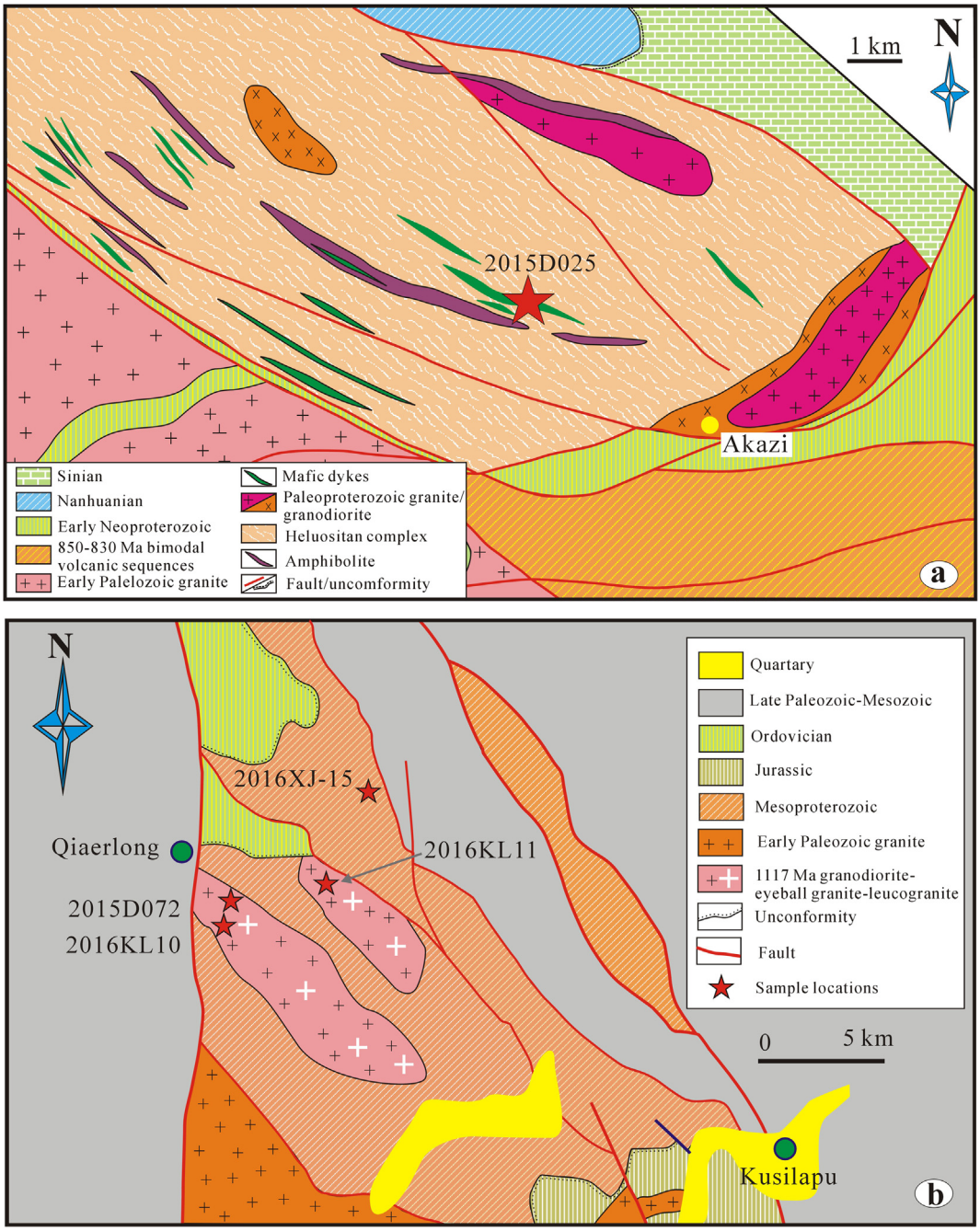

Fig. 2. Geological maps of the ca. 1785 Ma mafic dykes emplaced in the Paleoproterozoic Heluositan complex (a) and the ca.1117 Ma granodiorite- augen granite-leucogranite emplaced in the Sangzhutage Group (b).

from sample 2015D025, nineteen analyses were carried out on 19 grains and the results show variable U, Th contents with Th/U ratios ranging from 0.04 to 0.9. Among them, most analyses exhibit variable radiogenetic lead lost as revealed by the replacement of the baddeleyite by zircon at the rim of some grains. Nevertheless, sixteen analyses define an acceptable Discordia with an upper intercept age of 1780 ± 12 Ma (Fig. 4a, MSWD = 0.62, N = 16). Wang et al. (2014) mentioned a ca.1.8 Ga zircon unpublished U-Pb age of the dykes without providing any data;, this age is consistent with the baddeleyite U-Pb age obtained in this study. Thus, we conclude that the mafic dykes crystallized at ca.1785 Ma.

5.1.2. Age of the meta-rhyolite from KG (Sample 2016KL02)

Zircons from the meta-rhyolite are colorless, euhedral and are 80–120 μm long. In CL images, a zoning texture is commonly seen, indicating a magmatic origin. Eighteen analyses show a variable abundance of U (98 ppm to 442 ppm) and Th (45 ppm to 643 ppm) and Th/U ratios of 0.4 to 1.1 (mostly higher than 0.6). All analyses show concordant results and yield a weighted mean $^{206}Pb/^{238}U$ age of 1524.7 ± 4.3 Ma (Fig. 4b) (95% confidence level, MSWD = 0.87). This is interpreted as a primary age of emplacement of bimodal volcanism in the Kalakashi Group (KG).

5.1.3. The age of the Sangzhutage Group (SZG)

Zircons from the four clastic rock samples of the SZG range from 80 μm to 200 μm in length and have length to width ratios of 1–3. In CL images, the detrital zircons show very different inner features to each other, some of them exhibit oscillatory zoning, similar to that of the

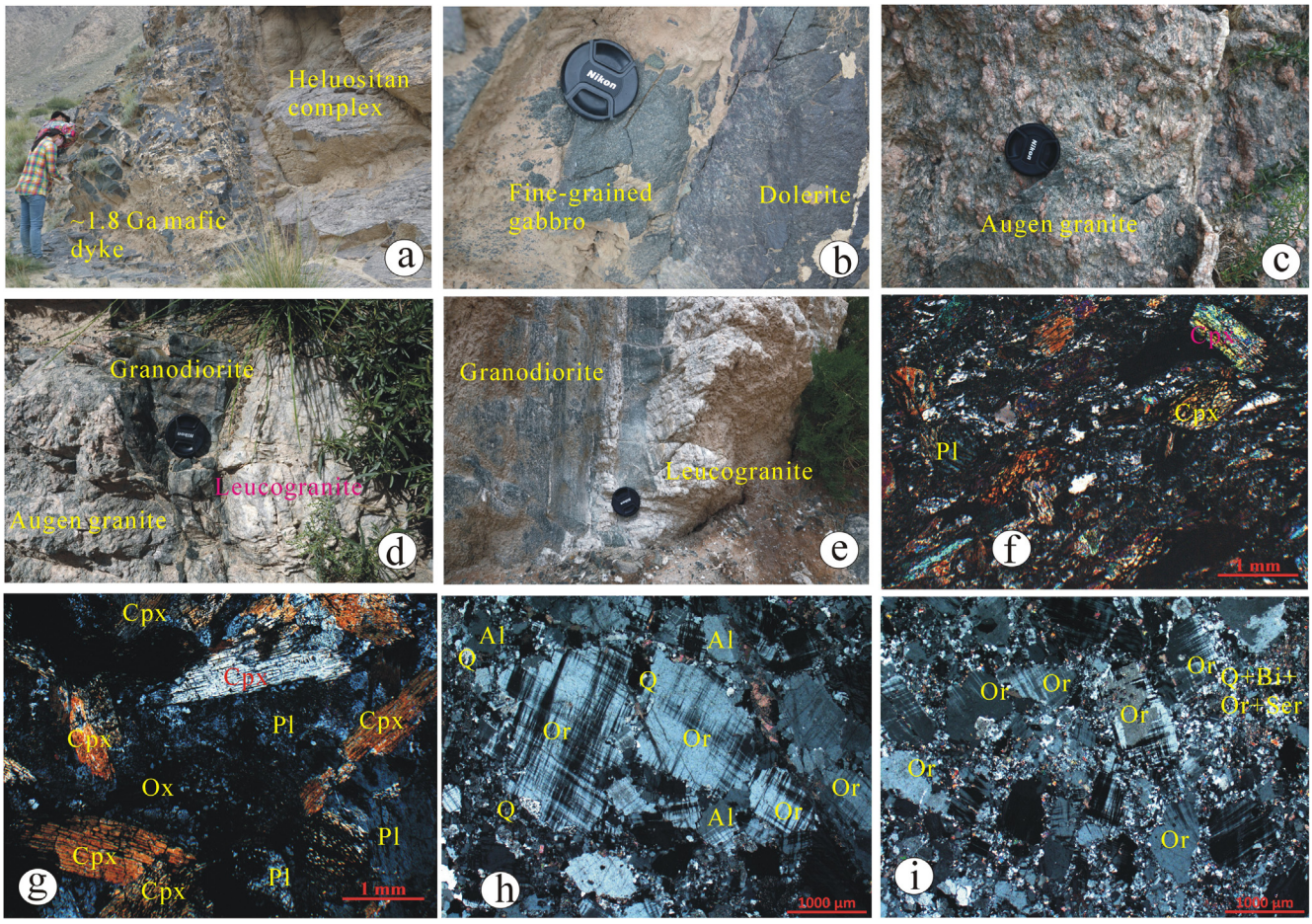

Fig. 3. Representative field and petrographic photographs of the studied mafic dykes and granitic intrusions. (a, b) the ca. 1785 Ma mafic dykes intruding the Heluositan gneiss; chilled margin can be seen. In the centre of a ca. 10 m wide dyke, from margin to centre, the mineral size increases gradually and fine-grained gabbro in the centre is seen; (c) augen granite; (d, e) intermingling structure between granodiorite, augen granite and leucogranite; (f, g) photomicrographs of the fine-grained gabbro (crossed polars and transmitted light); (h) photomicrographs of phenocrysts (orthoclase); subgranulation was observed (cross polars and transmitted light); (i) photomicrographs of the leucogranite; subgranulation was observed (cross polars and transmitted light). Pl-plagioclase, Cpx-clinopyroxene, Q-quartz, Or-orthoclase, Al-albite, Bi-biotite, Ser-sericite.

zircons crystallized from silicic magma, while others show homogenous or wide-striped inner structure, sharing some features of the zircons crystallized from mafic magma (Hoskin and Schaltegger, 2001). One hundred and four analyses were carried out on 104 zircon grains for sample 2016XJ-15. About a quarter of the analyzed zircons yield $^{206}Pb/^{207}Pb$ ages older than 1.6 Ga (Supplementary Table 1). The other seventy-nine analyses have broadly concordant and consistent ages around at ca.1460 Ma and they defined a Discordia with upper intercepted age of 1458 ± 14 Ma (N = 79, MSWD = 0.66) (Fig. 4c). Those analyses yield a mean $^{206}Pb/^{207}Pb$ age of 1467.7 ± 5.5 Ma (N = 79, MSWD = 0.68). In line with the detrital zircon U-Pb ages and the 1.4 Ga granite intruding the SZG (Ye et al., 2016), we conclude that the SZG deposited during 1.5–1.4 Ga.

5.1.4. The age of the granodiorite - augen granite-leucogranite in qiaerlong

Zircons from sample 2015KL72 are of short columnar forms, transparent and colorless or slight yellowish, ranging from 80 μm to 150 μm in length, with length/width ratios of 1.5–2. Oscillatory zoning is commonly observed in CL images. Thirty-seven analyses were conducted on 37 zircon grains. Six spots yield younger $^{206}Pb/^{238}U$ ages possibly due to variable radiogenic lead loss, but all the analyses define an excellent Discordia with an upper intercept age of 1117.8 ± 9.4 Ma (MSWD = 0.26, N = 37) (Fig. 4d). On the other hand, all the analyses yield consistent $^{207}Pb/^{206}Pb$ ages with a weighted average value of 1116 ± 9.4 Ma (MSWD = 1.08, N = 37). Thus, the augen granites crystallized at ca.1117 Ma.

Zircons from the granodiorite and leucogranite samples are transparent, colorless and of 60–120 μm in length. In CL images, oscillatory zoning is commonly seen in most zircon crystals, indicating their crystallization from silicic magma (Hoskin and Schaltegger, 2001). Core-mantle structure was occasionally observed in CL images. Twenty and eighteen analyses were performed for sample 2016KL10 and 2016KL11, respectively. Most analyses yield concordant $^{206}Pb/^{238}U$ and $^{207}Pb/^{235}U$ ages with a few spots having slight radiogenic lead loss. Nevertheless, all the analyses share consistent $^{207}Pb/^{206}Pb$ ages within analytical errors and they yield weighted mean $^{207}Pb/^{206}Pb$ ages of 1118 ± 5 Ma (MSWD = 0.6, N = 19) and 1116 ± 0.6 Ma (MSWD = 0.51, N = 17), respectively (Fig. 4e, f). Thus, the augen granites, granodiorites and leucogranites were coevally emplaced.

5.2. Whole-rock geochemistry

5.2.1. The ca. 1785 Ma mafic dykes in yecheng

The ca. 1785 Ma mafic dyke samples have similar major elements compositions with SiO_2 ranging from 49% to 50% except one sample (2016KL05H5), which has significant lower SiO_2 and extremely high LOI (11.45%), due to carbonate alteration (Supplementary Table 3). Due to the concerns regarding alteration, we use immobile elements for the rock classification. As shown in Fig. 5a, all the samples have a subalkaline basalt signature in the Zr/TiO_2 versus Nb/Y diagram

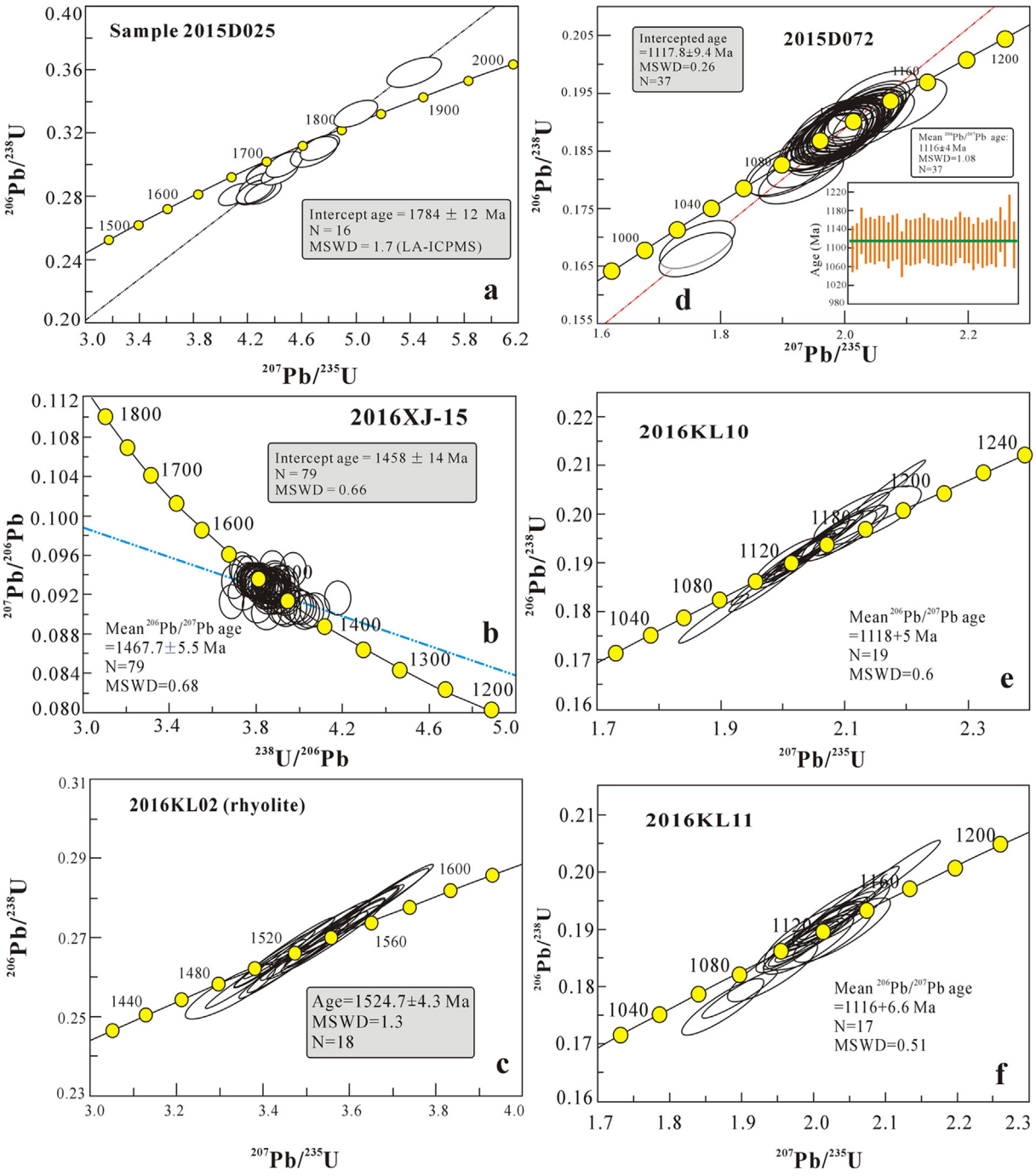

Fig. 4. Concordia of U-Pb zircon data for the baddeleyite from the mafic dykes, the meta-rhyolite from Kalakashi Group and the granodiorite- augen granite-leucogranite (see details in the text).

(Winchester and Floyd, 1977). In line with their FeO^T/MgO ratios and TiO_2 contents, they exhibit a typical tholeiitic trend (Figure not shown).

The mafic dykes have low compatible element contents, such as Cr with values mostly lower than 100 ppm, except for the sample 2016KL05H5 (Cr = 401 ppm), Ni from 8 to 123 ppm, Sc from 12 to 58 ppm, Co from 30 to 273 ppm, and V from 10 to 292 ppm (Supplementary Table 3). This indicates that fractionation/cumulation of mafic minerals are the main factors controlling the compatible element abundances due to the absence of any sulphide in the dolerites/gabbros. LREEs are uniformly enriched relative to HREEs with consistent $(La/Yb)_N$ ranging from 2 to 4. They show insignificant Eu anomalies with Eu/Eu* ratios ranging from 0.97 to 1.07 (Fig. 6a) (both chondrite and primitive mantle values are from Sun and McDonough, 1989). Primitive mantle normalized spider diagrams for incompatible elements also exhibit variable abundances (Fig. 6b). They are anomalously enriched in Rb and Ba with negligible Nb-Ta troughs and Nb/La ratios ranging from 0.86 to 1.08. Slightly positive or negative P and Ti anomalies were observed on the PM-normalized diagrams, indicating fractionation/cumulation apatite and Ti-bearing minerals (such as rutile and/or Ti-magnetite) (Fig. 6b).

5.2.2. *The ca. 1117 Ma granitic intrusions*

Due to their close spatial and temporal relations of the granodiorite, augen granite and leucogranite, the ca.1117 Ma intrusions could share a common magma source and the diverse rock types were induced by crystal fractionation. Overall, the samples have SiO_2 ranging from 66%

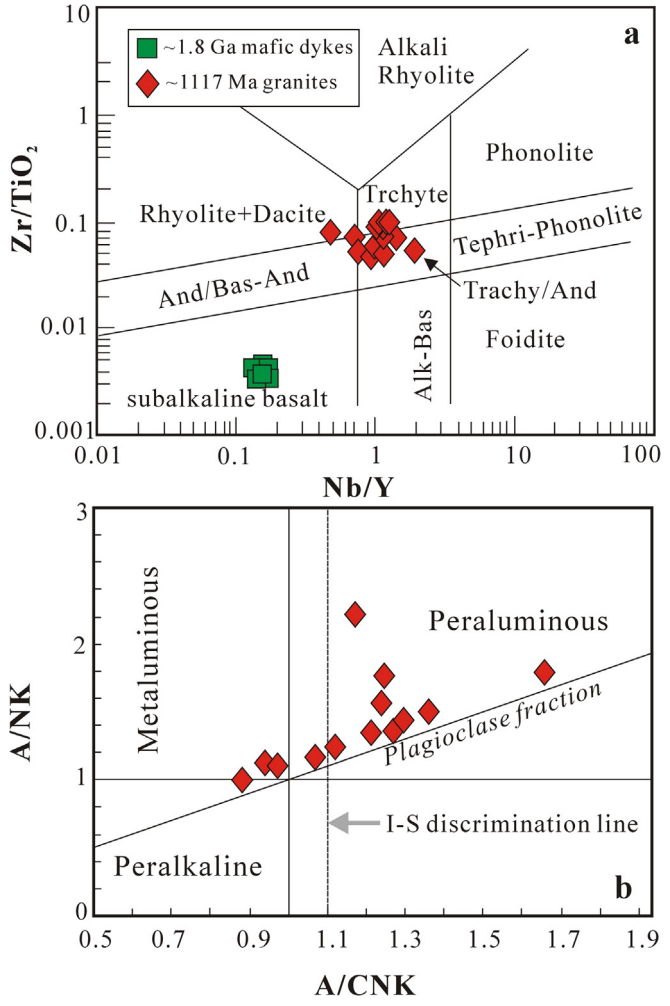

Fig. 5. (a) Nb/Y vs. Zr/TiO_2 classification diagram of the ca. 1785 Ma mafic dykes and the ca. 1117 Ma granitic rocks; (b) A/CNK-A/NK diagram showing the fractionation of plagioclase for the ca. 1117 Ma granitic rocks.

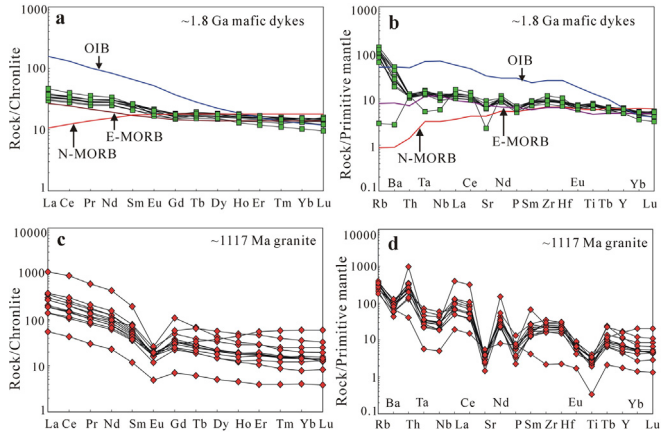

Fig. 6. Chondrite-normalized REE patterns and Primitive mantle -normalized incompatible elements spider diagrams of ca. 1785 Ma mafic dykes and the ca. 1117 Ma granitic rocks. OIB, E-MORB and N-MORB are also presented for comparison (both Chondrite and Primitive mantle values, OIB, E-MORB and N-MORB are from Sun and McDonough, 1989).

to 77% (volatile free), variable K_2O (3.0–8.0%), MgO (0.15–4.94%), $Fe_2O_3^T$ (0.9–5.3%), Al_2O_3 (11.7–16.1%), CaO (0.4–3.2%) and TiO_2 (0.07–0.94%) contents. K_2O content is generally higher than that of Na_2O and their total alkalis ranges from 8.4% to 10%. As shown in the Nb/Y vs. Zr/TiO_2 diagram (Fig. 5a), most samples straddle between foidite and trachyte, indicating their alkaline character. Their major elements define a meta-aluminous to peraluminous nature with A/CNK values of 0.9–1.7 (Fig. 5b). On the Harker diagrams, as SiO_2 increases, MgO, $Fe_2O_3^T$ and MnO decrease, while Zr, Sr and TiO_2 show insignificant correlation with SiO_2. As for Al_2O_3 and CaO, they show inverse variation trends, as SiO_2 increases from 66% to 70%, Al_2O_3 increases, while CaO decreases. When SiO_2 is higher than 70%, Al_2O_3 decreases while CaO increases (Supplementary Fig. 2). As for trace elements, they have a large range of total REE contents (60–1164 ppm) and are enriched in LREE relative to HREE with high La_N/Yb_N ratios ranging from 5 to 55 (mostly between 10 and 20). They show significant and variable negative Eu anomalies (δEu = 0.2–0.6) (Fig. 6c). On the trace element spider diagram normalized by primitive mantle, the rocks are systematically depleted in Nb, Sr, P and Ti and show a significant Nb-Ta trough (Nb/La = 0.1–0.5) (Fig. 6d).

5.3. Baddeleyite/zircon Hf isotope compositions

Baddeleyite grains from the ca. 1785 Ma mafic dyke have constrained $^{176}Hf/^{177}Hf$ ratios from 0.281791 to 0.281922 and very low $^{176}Yb/^{177}Hf$ ratios (Supplementary Table 2). As shown on Fig. 7a, their εHf(t) values range from 4 to 7 with $T_{DM}(Hf)$ from 1.9 Ga to 2.1 Ga.

Despite only sixteen analyses for the zircons of the ca. 1525 Ma meta- rhyolite from KG, these data have a relatively large range of εHf (t) values ranging from −3.5 to 3.4 (Fig. 7a). Nevertheless, they show a

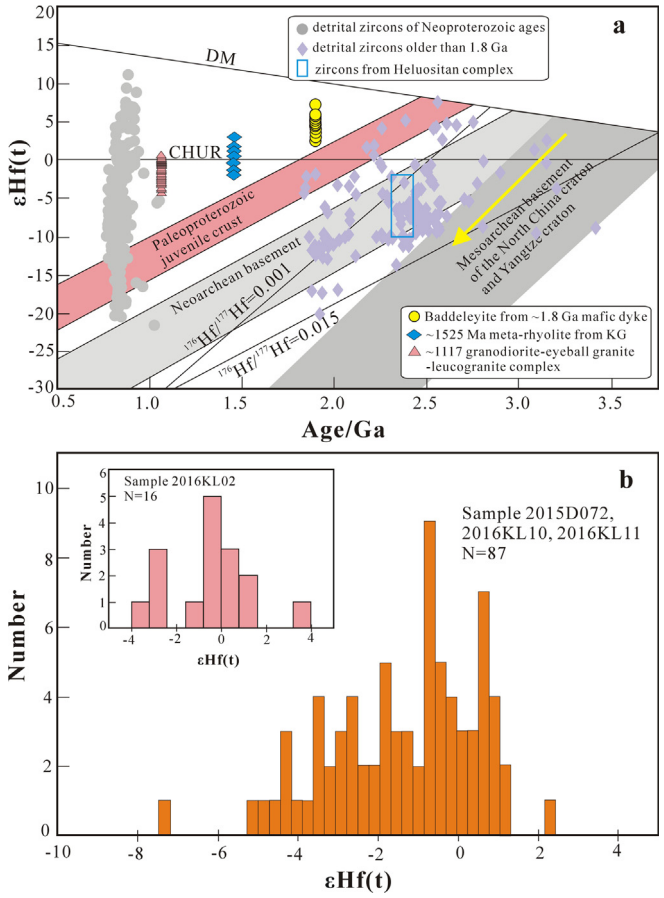

Fig. 7. Crystallization age vs. εHf(t) diagram (a) and histogram of the εHf(t) values of the ca.1525 Ma meta-rhyolite from KG and the ca.1117 Ma granitic rocks (b). The detrital zircon data from the Neoproterozoic sequences in STT is from Zhang et al. (2016). The range of the εHf(t) values of the zircons from Heluositan complex and the ~ 1.4 Ga A-type granites is after Ye et al. (2016) (see details in the text).

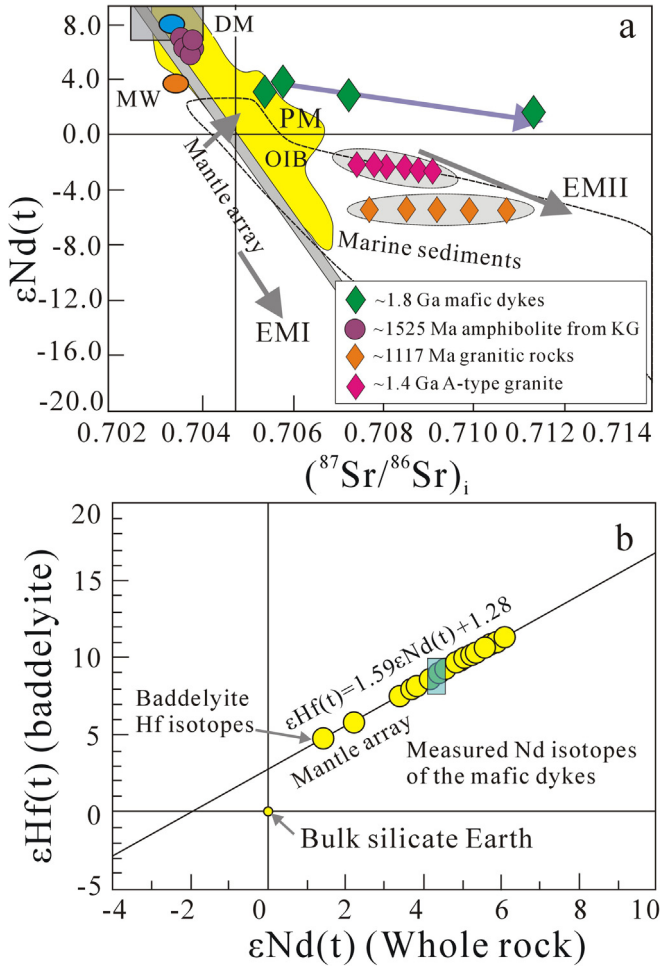

Fig. 8. (a) εNd(t) vs. $(^{87}Sr/^{86}Sr)_i$ diagram (due to the hydrothermal alteration and high Rb/Sr ratios, the $(^{87}Sr/^{86}Sr)_i$ values are meaningless for the ca. 1117 Ma granitic rocks and ca. 1.4 Ga A-type granite); (b) $\varepsilon Hf(t)_{baddelyite}$ vs. $\varepsilon Nd(t)_{whole\text{-}rock}$ diagram showing their broadly coupled Nd-Hf isotope compositions of the ca. 1785 Ma mafic dykes (mantle array is from Chauvel and Blichert-Toft, 2001).

broad Gaussian distribution (inset of Fig. 7b).

Zircons from the three samples of the ca. 1117 Ma granodiorite-augen granite -leucogranite show a large range in $^{176}Hf/^{177}Hf$ ratios from 0.281885 to 0.282170. All the analysed spots have low $^{176}Lu/^{177}Hf$ and $^{176}Yb/^{177}Hf$ ratios (Supplementary Table 2), indicating the validity for petrogenecitc discussion (Griffin et al., 2000; Wu et al., 2006). The zircons range in εHf(t) values from −7.3 to 2.2 (Fig. 7a). After excluding two spots of the lowest and highest εHf(t) values, the others have constrained εHf(t) values between −5 to 1.5, and show a broad Gaussian distribution on the histogram of εHf(t) with values peaking at ~ −1.5 (Fig. 7b). Their model ages T_{DM}^{C} cluster around from 2.1 to 2.6 Ga.

5.4. Whole-rock Sr-Nd isotope compositions

Sr-Nd isotope compositions, as well as the calculated $(^{87}Sr/^{86}Sr)_i$, εNd(T) and Nd model ages T_{DM} of the ca. 1790 Ma mafic dyke and ca. 1117 Ma granites are reported in Supplementary Table 4 and Fig. 8a. The mafic dyke samples have a large range of measured $^{87}Sr/^{86}Sr$ (0.7294–0.7484) and $^{143}Nd/^{144}Nd$ (0.512661–0.512732) ratios, corresponding to $(^{87}Sr/^{86}Sr)_i$ ranging from 0.7062 to 0.7084 and εNd(t) values (T = 1.8 Ga) from 1.95 to 4.49, respectively. Nevertheless, except for sample 2015KL05H6, the other three samples have consistent Nd-Sr isotope compositions. According to the mantle array of the Nd-Hf isotope compositions (Blichert-Toft and Albarède, 1997; Chauvel and Blichert-Toft, 2001), the mafic dykes have broadly coupled whole-rock Nd and zircon Hf isotope compositions (Fig. 8b).

Due to the hydrothermal alteration and the high Rb/Sr ratios of the ca. 1115 Ma granitic rocks, their large range of $(^{87}Sr/^{86}Sr)_i$ ratios are unsuitable for further discussions (e.g., McCulloch et al., 1981; Zou et al., 2004) (Supplementary Table 4). Nevertheless, they have constrained εNd(t) values ranging from −5.5 to −5.2 (Fig. 8a).

6. Petrogenesis

6.1. Petrogenesis of the ca. 1790 Ma mafic dyke swarm

The mafic dykes might have undergone AFC (Assimilation Fractional Crystallization) effect, given their low $Mg^{\#}$ (45–56) and low Cr (74–117 ppm), Ni (55–71 ppm) contents (the carbonate-altered sample 2016KL05H5 is excluded). The well-defined negative correlation between CaO, Al_2O_3, MgO with SiO_2 reveals fractionation of olivine and clinopyroxene (Figures not shown). The lack of significant Eu anomalies precludes the fractionation/cumulation of plagioclase during magma evolution.

The mafic dykes exhibit trace element signatures similar to those of intraplate basalts, rather than volcanic arc basalts according to their enrichment of LREE and insignificant Nb-Ta trough on the incompatible element spider diagram (Fig. 6a, b). Due to their similar partition coefficients of HFSEs, their ratios could be used to decipher their mantle sources. In Fig. 9, the mafic dykes have almost identical Nb/La, Th/La, Ce/Nb and Th/Nb ratios to those of the E-MORB, suggesting that their primitive magmas were derived from an asthenospheric mantle source rather than a metasomatized SCLM source. Moreover, they have significantly radiogenic whole rock Nd isotope compositions (εNd(t) = ~4) coupled with depleted baddeleyite Hf isotope compositions (εHf (t) = 3–7). All those features unambiguously argue for their asthenospheric mantle sources. Excluding the carbonated sample (2016KL05H5), all the other samples show consistent REE and incompatible elements distribution patterns and consistent whole rock Nd isotope compositions; thus we conclude that crustal contamination was negligible. The mafic dykes have restricted La_N/Sm_N and Sm_N/Yb_N ratios (La_N/Sm_N = 1.5–1.6, Sm_N/Yb_N = ~1.7). According to the REE modelling, they were derived from 10 to 15% degree of partial melting of garnet-bearing spinel peridotite (Workman and Hart, 2005). In summary, we suggest that the parental magma of the mafic dykes was derived from an E-MORB like mantle source without significant crustal contamination.

Besides their typical intraplate geochemical features (Fig. 6a, b; Fig. 10), the mafic dykes have high Fe/Mn ratios (60–71). Amongst the basaltic rocks formed in distinct settings, most MORB have Fe/Mn ratios around 55–59, comparable with Fe/Mn = 54–59 of island arc basalts, whereas OIB usually have Fe/Mn greater than 60. Several studies have suggested that high Fe/Mn is characteristic of plume-derived magmas (Humayun et al., 2004; Lee, 2004; Li et al., 2005a,b, 2006). The mafic dykes and basalts have a comparable Fe/Mn ratio with those of the Hawaiian OIB (Li et al., 2006). Though we are not able to establish their affinity to plume-derived magma, these rocks were formed in an extensional tectonic setting with a high degree of partial melting.

6.2. Petrogenesis of the ~1117 Ma granitic intrusions

In line with their petrography, the granitic samples have major- and trace element geochemical characteristics resembling those of A-type granites, such as having high total alkali and high-field-strength element contents. In the 10,000 × Ga/Al vs. Zr diagram (Fig. 11a), all samples fall in the A-type field (Whalen et al, 1987). The granites have high Nb contents, falling exclusively in the A2-type granite field in the Nb-Y-Ce ternary diagram (Fig. 10b; Eby, 1992) and into the field of within-plate granites in the plots of Nb vs. Y and Rb vs. (Y + Nb)

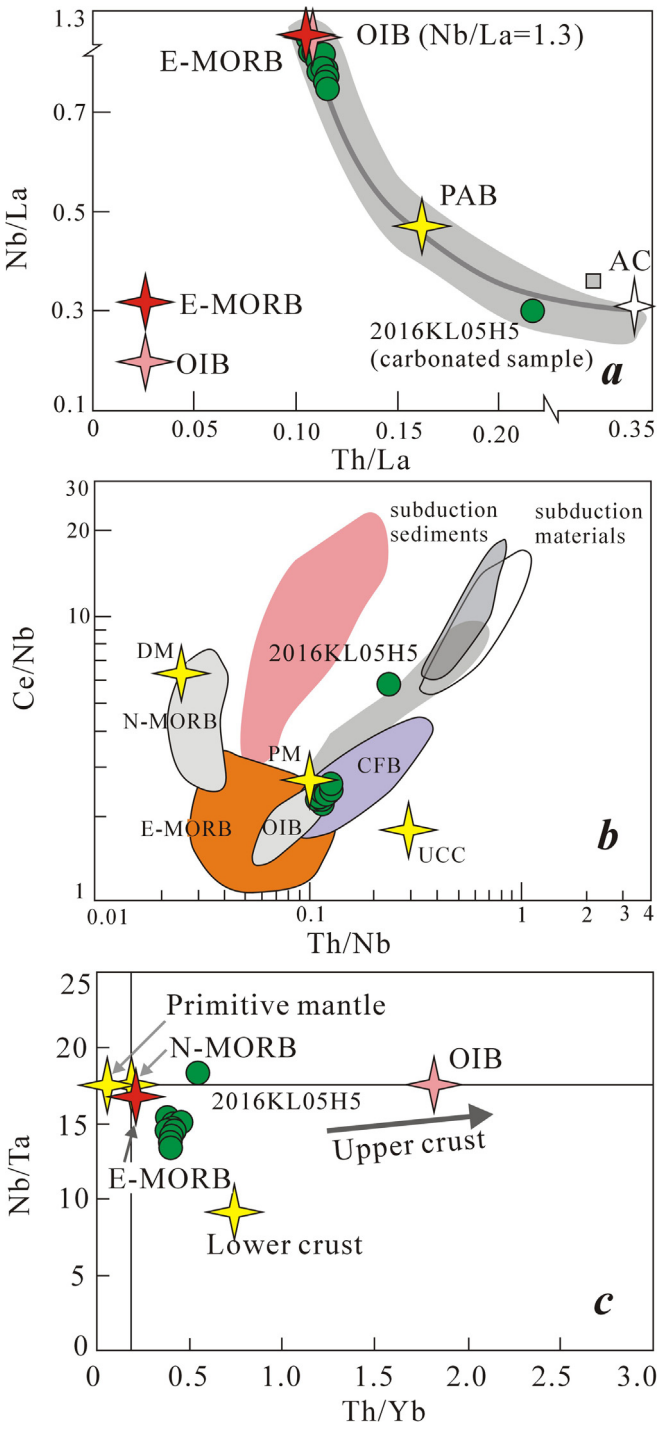

Fig. 9. Nb/La vs. Th/La, Th/Nb vs. Ce/Nb and Th/Yb vs. Nb/Ta diagrams showing that most mafic dyke samples share features with E-MORB (after Pearce, 2008, 2014; see details in the text).

(Fig. 11c, d, Pearce et al., 1984). Several petrogenesis models suggest that mantle-derived mafic magma could be variably involved in the genesis of the A-type granites (e.g., Collins et al., 1982; Whalen et al., 1987; Sylvester, 1989; Eby, 1992; Bonin, 2007). However, due to significant less radiogenetic Nd isotope compositions (εNd (t) = −5 ~ −5.5) and no coeval mafic rocks identified in STT, we consider a petrogenetic model involving melting of crustal sources to be more likely in this case. Furthermore, the consistent Nd isotopes and zircon Hf isotopes revealed that their primitive magma was most likely derived by partial melting of a Paleoproterozoic crust such as the

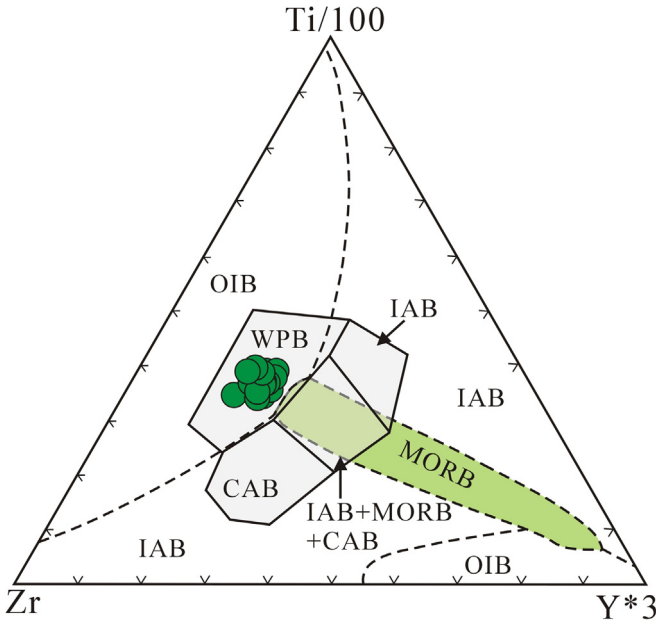

Fig. 10. Ti/100-Zr-Y*3 triangle diagram showing the typical intraplate signature of the ca. 1785 Ma mafic dykes (after Pearce, 2008). The dashed line is after Vermeesch (2006).

Heluositan complex in STT (Zhang et al., 2007; Ye et al., 2016). The whole-rock Nd model ages of the granitic rocks range from 2.0 to 2.5 Ga, implying that the early Paleoproterozoic lower crust could be a potential source for the granites. On the other hand, due to the low SiO_2 contents of the granodiorite samples, high alkali, REE and HFSE contents and decoupled Nd-Hf isotope between the ca. 1117 Ma A-type granites and the Paleoproterozoic granitic gneiss (Ye et al., 2016), the silicic member of the Heluositan complex is unsuitable for the magma source (Whalen et al., 1987). Previous work has shown that the mafic unit in the Heluositan complex has an initial $\varepsilon_{Nd}(t)$ value of +2.15 at ~2.4 Ga (Zhang et al., 2007), corresponding to a $\varepsilon_{Nd}(t)$ value of −5.0 at ca. 1117 Ma. The recalculated Nd isotopic composition is within the range of $\varepsilon_{Nd}(t)$ values (−5.0 to −5.5) of the granitic rocks. Petrographic observations revealed that some of the mafic members in Heluositan complex could be mafic intrusions mingled into the silicic member after their emplacement, it is reasonable to deduce that there exists early Paleoproterozoic mafic lower crust beneath the STT. Thus, Nd isotope compositions reveal that the granitic intrusions originated mainly from partial melting of the early Paleoproterozoic mafic lower crust.

7. Precambrian tectonic evolution of the STT

7.1. The assemblage of STT to the Columbia

As mentioned earlier, the 2.41–2.34 Ga Heluositan complex is the oldest crystallized basement identified in STT. Both in the granitic member and gneissic mafic member, a ca. 1.9 Ga reworking event has been demonstrated by geochronological studies and among them, the most precise age is 1907 ± 6 Ma obtained from the 2.41 Ga Akazi pluton by the SHRIMP method (Fig. 12, Zhang et al., 2007; Wang et al., 2014; Ye et al., 2016). In the Neoproterozoic sedimentary sequences, ca. 1.9 Ga detrital zircons are commonly seen (Zhang et al., 2016). It is reasonable to deduce that the STT had assembled to the Columbia supercontinent at ca. 1.9 Ga, or alternatively, it could be a continental fragment detached from a Columbian continent and only accreting later (Fig. 12).

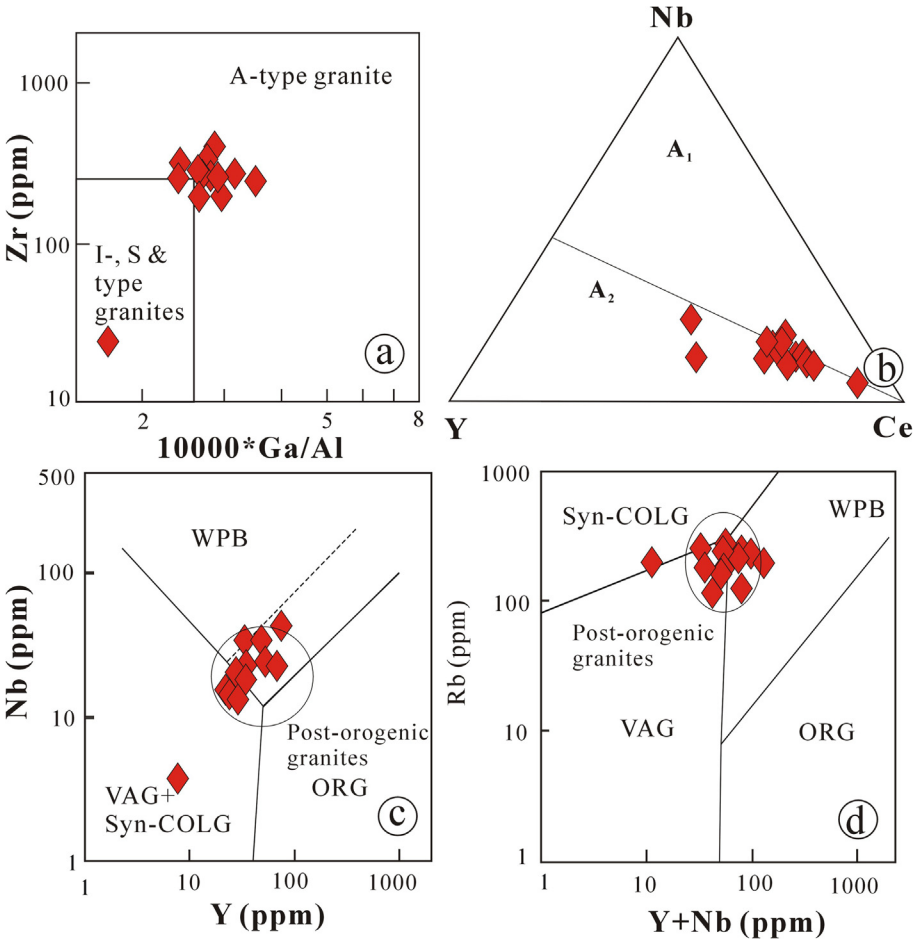

Fig. 11. (a) Zr vs. 10,000 × Ga/Al diagram of Whalen et al. (1987), showing the A-type nature of the ca. 1117 Ma granitic rocks; (b) Nb-Y-Ce diagram of Eby (1992) showing data points for the ca. 1117 Ma granitic rocks within the A2 subtype of the A-type granites; (c) and (d) Nb vs. Y and Nb + Y vs. Rb plots of Pearce et al. (1984), showing that the ca. 1117 Ma granitic rocks plot in the field of post-orogenic granites (see details in the text).

7.2. Breakup of the STT from the Columbia supercontinent to its assemblage in Rodinia

The newly identified ca. 1785 Ma mafic dyke swarm intruding the Heluositan complex shows significant intraplate geochemical features (Fig. 10). The primitive magma of the mafic dykes was derived from 10 to 15% degree partial melting of a depleted asthenospheric mantle. Globally the ca.1.8 Ga igneous activities have been well documented in many Columbian continents such as the North China, Baltica, Australia, India, West Africa, Amazonia (Ernst et al., 2008, 2013 and references therein; Peng, 2010; Baratoux et al. 2019). These matches could imply a reconstruction adjacent to some of these blocks. In particular, links with the North China craton and the West African craton are particularly interesting, the latter because the 1525 Ma age mentioned below has a rather unique age match with a LIP in the southern West African craton (Baratoux et al. 2019). We infer that the ca. 1785 Ma mafic dykes in the STT represented the initial breakup event affecting the STT.

The Mesoproterozoic sequences in STT include the lower member KG and the upper member SZG. The lower member KG is mainly composed of amphibolite-facies metamorphic bimodal volcanic rocks (herein dated at 1525 Ma) and clastic sedimentary sequences (Fig. 12). The amphibolites (basalts) show E-MORB geochemical signatures such as their E-MORB like REE patterns, high Nb/La ratios (0.6–1.1) and depleted Nd isotope compositions ($\varepsilon Nd(t) = 7.5–5.5$, $t = 1525$ Ma) (Fig. 8a; recalculated using the data from Zhang et al., 2003). An intraplate age of 1525 Ma is only recognized in the West African and formerly connected Amazonia cratons. Recently U-Pb ID-TIMS dating has revealed a widespread 1525 Ma LIP in the West African craton (the 1525–1529 Ma Essakane swarm, and 1521 ± 3 Ma Sambarabougou swarm, and extending into formerly adjacent Amazonian craton (1528 ± 2 Ma Kayser dykes) (Baratoux et al. 2019).

1110–1120 Ma intraplate mafic magmatism is present on various crustal blocks and represents fragments of LIPs. Specifically this includes the Kalahari craton, S. Africa (Umkondo LIP); Dronning Maud Land, Antarctica; Bundelkhand craton, India (Mahoba dykes); Congo craton (Epembe-Huila dykes and sills); and Amazonia craton (Rincon del Tigre-Huanchaca sills and Rio Perdido dykes) (Ernst et al. 2013; de Kock et al. 2014; Moabi et al. 2017; Teixeira et al. 2018; Salminen et al. 2018), and also in the Mid-Continent region of North America (Keweenawan LIP). These (apart from the Keweenawan LIP) have been reconstructed as a single LIP (Ernst et al. 2013; de Kock et al. 2014) with plume centre beneath the Kalahari craton. A revised and improved reconstruction of Kalahari being adjacent to Congo craton is proposed by Salminen et al. (2018) on the basis of new paleomagnetic data on the Epembe dykes of the Congo craton with the Umkondo magmatism of the Kalaharic craton. The ca. 1117 Ma granitic complex in STT could be part of the above mentioned plume- related LIP which induced the final breakup of the Columbia supercontinent.

As for the temporal overlapping between the breakup of the Columbia and the assemblage of the Rodinia supercontinents, the dispersing of the STT from a Precambrian craton could take place at ca. 1.5 Ga in line with the intensively depleted signature of the basalts from KG, which possibly indicated a nascent ocean basin (Zhang et al., 2003). The STT most likely docked at the northern fringe of Australia

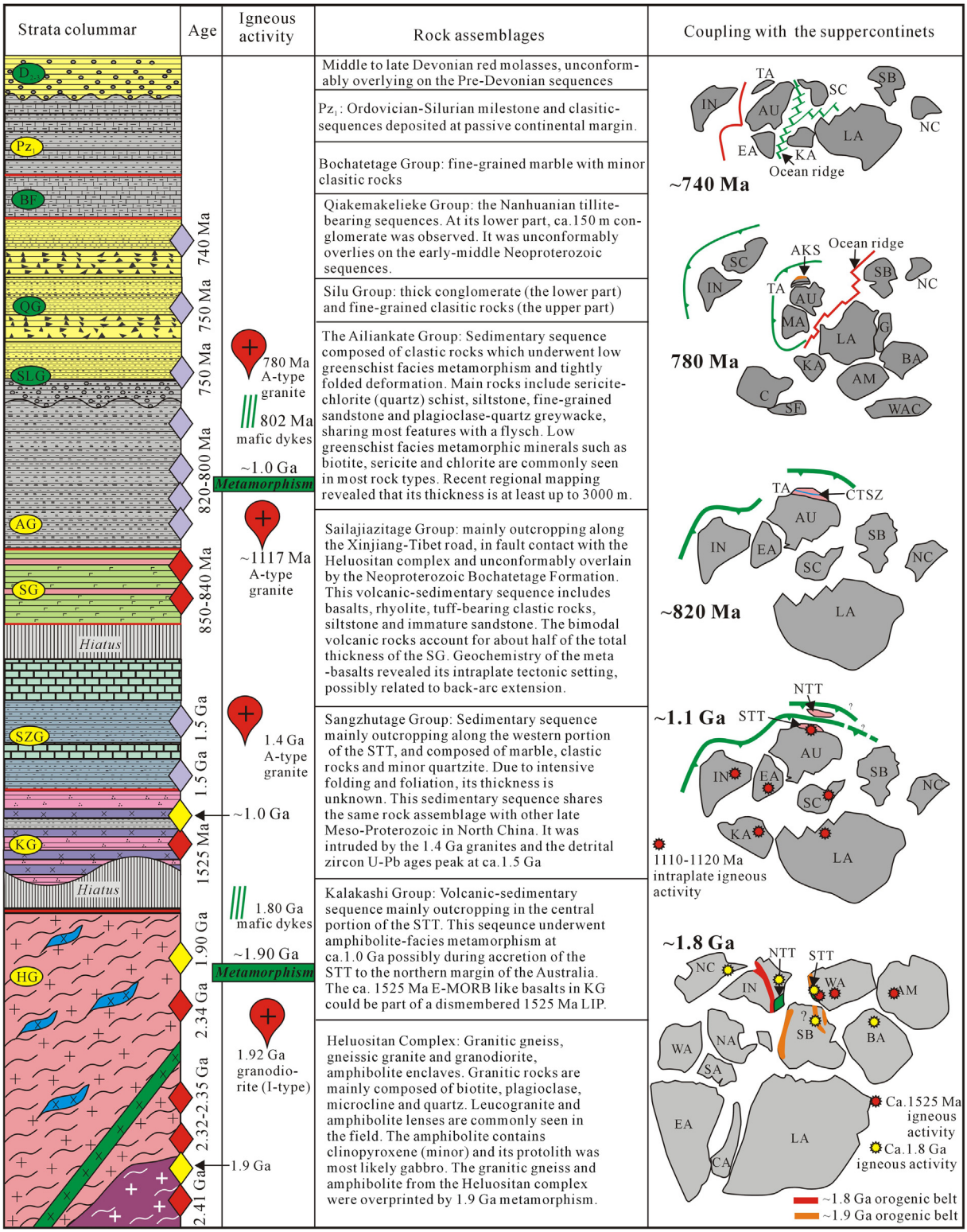

Fig. 12. A schematic diagram to illustrate the rock packages, Precambrian tectonic evolution process and its coupling with the global Precambrian supercontinent evolution of the STT. The configuration of the ca.1.8 Ga Columbia supercontinent is after Zhang et al. (2012a) and the configuration of the Rodinia supercontinent as well as its breakup process is after Li et al. (2008). The red diamond represents ages of the igneous rocks, the purple diamond represents the detrital zircon U-Pb age from the clastic rocks (the youngest population) while the yellow diamond represents metamorphic ages. LA-Laurentia, BA-Baltica, SB-Siberia, WA-Western Africa, AM-Amazonia, EA-eastern Antarctica, NC-North China, NA-North Australia, SA-South Australia, WA-West Australia, IN- India, SC-South China, STT-southern Tarim terrane, NTT-northern Tarim terrane, C-Congo, KA-Kalahari, AU- Australia, CTSZ-central Tarim suture zone (820–800 Ma), TA-Tarim. HG-Heluostan compelx, KG-Kalakashi Group, SZG-Sangzhutage Group, SG-Sailajiazitage Group, AG-Ailiankate Group, SLG-Silu Group, QG-Qiakemakelike Group, BF-Bochatetage Formation, Pz_1-lower Paleozoic, $D_{2\text{-}3}$- middle to upper Devonian. (For interpretation of the references to color in this figure legend, the reader is referred to the web version of this article.)

during the assemblage of Rodinia as demonstrated by the ~ 1.0 Ga metamorphism of the KG (Fig. 12, Zhang et al., 2003; Li et al., 2008; Cawood et al., 2013).

7.3. The Neoproterozoic evolution of the STT

In line with the E-W aeromagnetic anomaly belt cross the central Tarim, most geologists argued for a Precambrian suture zone in central Tarim (Yin and Nie, 1996; Wu et al., 2012; Xu et al., 2013a). In recent years, the stratigraphic framework identified by the drill cores and seismic data unambiguously demonstrated that the Nanhuaian-Cambrian sequences unconformably overlie the pre-Nanhuaian metamorphic and folded rocks (Xu et al., 2013a). Furthermore, geochemical data of the samples of the early Neoproterozoic granitic rocks fromdrill core in central Tarim defined their arc signatures (Li et al., 2003, 2005; Xu et al., 2013a). Thus, we interpret that the STT and the NTT unified together along the central Tarim suture zone in the middle Neoproterozoic (ca. 820 Ma). After the STT amalgamated with Australia at ca. 1.0 Ga, the south-dipping subduction along the central Tarim suture led to development of a nascent back-arc basin in the STT as represented by the 850–840 Ma SG volcanic-sedimentary sequence (Fig. 12, Yuan et al., 2004). As the NTT and STT amalgamated together along the central Tarim suture zone, at this time in STT, transformation from extension to compression induced the formation of the foreland basin on the previous back-arc sequence (i.e., the AG clastic rocks). At the same time, the Aksu Group volcanic-clastic rocks were deposited at a forearc basin (Zhang et al., 2014b). The low greenschist facies metamorphism and folding of the foreland basin package (AG) took place at ca. 780–760 Ma, geodynamically related to the blueschist facies metamorphism of the Aksu Group in the northern margin of the Tarim Block (Liou et al., 1996; Yong et al., 2013; Zhang et al., 2014b). After the formation of the uniform basement of the Tarim Block at ca.760 Ma, a passive margin and/or rift basins developed, and this tectonic setting continued, at least, till Cambrian, forming the middle Neoproterozoic to Cambrian cover sequence (unmetamorphosed and undeformed) over the entire Tarim Block, consistent with the breakup of the Rodinia supercontinent (Fig. 12, Li et al., 2008 and references therein).

7.4. The distinct feature of the STT and the NTT

Global-scale 2.1–1.8 Ga collision events have been well documented in a number of large continental cratons, and are linked with the assembly of the Columbia supercontinent (Rogers and Santosh, 2002; 2009; Zhao et al., 2002, 2011, 2012). Temporally the breakup process of the Columbia supercontinent overlapped with the assembly of the Rodinia supercontinent.

In comparison with the timing of the Columbia supercontinent assembly and crustal growth processes, the STT is most possibly closest to Laurentia or Siberia or West Africa (see details in Ye et al., 2016). In line with the distinct late Paleoproterozoic metamorphic event (ca.1.9 Ga), the initial breakup event at ca. 1790 Ma, the rare ca. 1525 Ma LIP and the global scale dismembered 1110–1120 Ma LIP, we speculate that the STT could be a continental fragment detached from West Africa, a suggestion that warrants further study. Though at present it is difficult to correlate the STT with Siberia or West Africa (Ye et al., 2016), it is obvious that the STT does not show any affinities with the NTT (Zhang et al., 2012c) and the terranes distributed to the southeast of STT, such as the Qaidam, Qilian and Alashan, show significant affinity with the Yangtze (Zhang et al., 2014a). Precambrian rock packages, tectono-magmatic events and crustal growth process unambiguously argue that the NTT shows significant affinity with crustal blocks of the India or/and North China (Zhao et al., 2011 and references therein). Notably, the STT is different from both the North China Craton and Yangtze Block.

In summary, the lack of synchronous nature in the late Paleoproterozoic orogenic events, as well as the differences in continental growth processes within the NTT and STT, provide further confirmation that the Precambrian basement of the Tarim Block is composed of two discrete terranes that did not amalgamate until early Neoproterozoic, during the assemblage of the Rodinia supercontinent (Fig. 12).

8. Conclusions

(1) Through U-Pb dating we demonstrate three phases of extension-related igneous activity in the STT, i.e., the ca. 1790 Ma mafic dykes, ca. 1525 Ma bimodal volcanic rocks and ca.1117 Ma granitic intrusions. These three phases of igneous activities could be genetically related to global LIPs during the breakup of the Columbia.
(2) The STT was possibly a continental fragment detached from West Africa (based on a magmatic age matches at 1790 and 1525 Ma), while the NTT could be a continental fragment from the North China or/and India. Both the STT and the NTT were involved in the global 2.1–1.8 Ga orogenic events leading to the formation of the Columbia supercontinent.
(3) The STT docked at the northern fringe of Australia at ca. 1.0 Ga. Then the STT and the NTT amalgamated together at ca.820 Ma along the central suture zone of the Tarim, this process led to the final formation of its Precambrian basement of the Tarim.
(4) The Tarim block may have bordered the circum-Rodinian ocean. The subduction along the northern margin of the Tarim could last till to 740 Ma and thereafter the Tarim dispersed from the Australia.

Acknowledgements

We sincerely thank Mr. Yu-Zhuang Zheng for his help with field work and supplying the 1/50000 geological maps. We are grateful to Dr. Xie Wei for his assistance with SHRIMP zircon dating, and to Prof. Hong-Ying Zhou for her help with baddeleyite/zircon Lu-Hf isotope analyses. This project is funded by the National 305 Project of China (2018A03004-1) and the Fundamental Research Fund for Central Universities (B16020127); R. Ernst has been partially supported from Mega-Grant 14.Y26.31.0012 of the Russian Federation.

Appendix A. Supplementary data

Supplementary data to this article can be found online at https://doi.org/10.1016/j.precamres.2019.01.018.

References

Baratoux, L., Söderlund, U., Ernst, R.E., de Roever, E., Jessell, M.W., Kamo, S., Naba, S., Perrouty, S., Metelka, V., Yatte, D., Grenholm, M., Diallo, D.P., Ndiaye, P.M., Dioh, E., Cournède, C., Benoit, M., Baratoux, D., Youbi, N., Rousse, S., Bendaoud, A., 2019. New U-Pb Baddeleyite Ages of Mafic Dyke Swarms of the West African and Amazonian Cratons: Implication for Their Configuration in Supercontinents Through Time. In: Srivastava, R.K., Ernst, R.E., Peng, P. (Eds.), Dyke Swarms of the World – A Modern Perspective. Springer, pp. 263–314.
Blichert-Toft, J., Albarède, F., 1997. The Lu-Hf isotope geochemistry of chondrites and the evolution of the mantle-crust system. Earth Planet Sci. Lett. 148, 243–258.
Black, L.P., Kamo, S.L., Allen, C.M., Davis, D.W., Aleinikoff, J.N., Valley, J.W., Mundil, R., Campbel, I.H., Korsch, R.J., Williams, I.S., Foudoulis, Chris, 2004. Improved $^{206}Pb/^{238}U$ microprobe geochronology by the monitoring of a trace-element-related matrix effect; SHRIMP, ID-TIMS, ELA-ICP-MS and oxygen isotope documentation for a series of zircon standards. Chem. Geol. 205, 115–140.
Bonin, B., 2007. A-type granites and related rocks: Evolution of a concept, problems and prospects. Lithos 97, 1–29.
Cawood, P.A., Wang, Y., Xu, Y., Zhao, G., 2013. Locating South China in Rodinia and Gondwana: a fragment of greater India lithosphere? Geology 41, 903–1875.
Cawood, P.A., Strachan, R.A., Pisarevsky, S.A., Gladkochub, D.P., Murphy, J.B., 2016. Linking collisional and accretionary orogens during Rodinia assembly and breakup: implications for models of supercontinent cycles. Earth Planet Sci. Lett. 449, 118–126.
Chauvel, C., Blichert-Toft, J., 2001. A hafnium isotope and trace element perspective on melting of the depleted mantle. Earth Planet Sci. Lett. 190, 137–151.
Collins, W.J., Beams, S.D., White, A.J.R., Chappell, B.W., 1982. Nature and origin of A-type granites with particular reference to southeastern Australia. Contrib. Mineral. Petrol. 80, 189–200.

Cumming, G.L., Richards, J.R., 1975. Ore lead ratios in a continuously changing Earth. Earth Planet Sci. Lett. 28, 155–171.
de Kock, M.O., Ernst, R.E., Söderlund, U., Jourdan, F., Hofmann, A., Le Gall, B., Bertrand, H., Chisonga, B.C., Beukes, N., Rajesh, H.M., Moseki, L.M., Fuch, R., 2014. Dykes of the 1.11 Ga Umkondo LIP, southern Africa: clues to a complex plumbing system. Precambrian Res. 249, 129–143.
Eby, G.N., 1992. Chemical subdivision of the A-type granitoids-petrogenetic and tectonic implications. Geology 20, 641–644.
Ernst, R.E., Wingate, M.T.D., Buchan, K.L., Li, Z.X., 2008. Global record of 1600–700 Ma Large Igneous Provinces (LIPs): Implications for the reconstruction of the proposed Nuna (Columbia) and Rodinia supercontinents. Precambrian Res. 160, 159–178.
Ernst, R.E., Pereira, E., Hamilton, M.A., Pisarevsky, S.A., Rodriques, J., Tassinari, C.C., Teixeira, W., Van-Dunem, V., 2013. Mesoproterozoic intraplate magmatic 'barco-de'record of the Angola portion of the Congo Craton: Newly dated magmatic events at 1505 and 1110Ma and implications for Nuna (Columbia) supercontinent re-constructions. Precambrian Res. 230, 103–118.
Feng, B.Z., Zhou, Y.W., Chi, S.F., 1995. Presinian geology, precious and nonferrous mental deposits in Quruqtagh area. In: Xinjiang Uygur Autonomous Region. Geological Publishing House, Beijing, China, pp. 23–125 (in Chinese).
Gao, Z.J., Chen, K.Q., 2003. The Nanhua system of Xinjiang and some geological issues of Nanhua system in China. Geol. Sur. Res. 26, 8–14 (in Chinese with English abstract).
Griffin, W.L., Pearson, N.J., Belousova, E., Jackson, S.E., Van Achterbergh, E., O'Reilly, S.Y., Shee, S.R., 2000. The Hf isotope composition of cratonic mantle: LAM-MC-ICPMS analysis of zircon megacrysts in kimberlites. Geochimica et Cosmochimica Acta 64, 133–147.
Guo, Z.J., Yin, A., Bobinson, A., Jia, C.Z., 2005. Geochronology and geochemistry of deep-drill-core samples from the basement of the central Tarim basin. J. Asia Earth Sci. 25, 45–56.
Hou, K.J., Li, Y.H., Tian, Y.R., 2009. In situ U-Pb zircon dating using laser ablation multi ion counting-ICP-MS. Min. Deposit. 28, 481–492 (in Chinese with English abstract).
Hoskin, P.W., Schaltegger, U., 2001. The composition of zircon and igneous and meta-morphic petrogenesis. Rev. Mineral. Geochem. 53, 25–104.
Humayun, M., Qin, L.P., Norman, M.D., 2004. Geochemical evidence for excess iron in the Hawaiian mantle: implications for mantle dynamics. Science 306, 91–94.
Lee, C.T., 2004. Are earth's core and mantle on speaking terms? Science 306, 64–65.
Li, Z.X., Bogdanova, S.V., Collins, A.S., Davidson, A., Waele, B. De, Ernst, R.E., Fitzsimons, I.C.W., Fuck, R.A., Gladkochub, D.P., Jacobs, J., Karlstrom, K.E., Lu, S., Natapov, L.M., Pease, V., Pisarevsky, S.A., Thrane, K., Vernikovsky, V., 2008. Assembly, con-figuration, and break-up history of Rodinia: a synthesis. Precambrian Res. 160, 179–210.
Li, Z.X., Zhong, S., 2009. Supercontinent–superplume coupling, true polar wander and plume mobility: Plate dominance in whole-mantle tectonics. Physics Earth Planet Inter. 176, 143–156.
Liou, J.G., Graham, S.A., Maruyama, S., Zhang, R.Y., 1996. Characteristics and tectonic significance of the late Proterozoic Aksu blueschists and diabasic dikes northwest Xinjiang, China. Inter. Geol. Rev. 38, 228–244.
Li, X.H., Liu, D.Y., Sun, M., Li, W.X., Liang, X.R., Liu, Y., 2004. Precise Sm-Nd and U-Pb isotopic dating of the super-giant Shizhuyuan polymetallic deposit and its host granite; Southeast China. Geol. Mag. 141, 225–231.
Li, X.H., Qi, C.S., Liu, Y., Liang, X.R., Tu, X.L., Xie, L.W., Yang, Y.H., 2005a. Petrogenesis of the Neoproterozoic bimodal volcanic rocks along the western margin of the Yangtze Block: new constraint from Hf isotopes and Fe/Mn ratios. Chinese Sci. Bull. 50, 2481–2486.
Li, X.H., Li, Z.X., Wingate, M.T.D., Chung, S.L., Liu, Y., Lin, G.C., Li, W.X., 2006. Geochemistry of the 755 Ma Mundine Well dyke swarm, northwestern Australia: part of a Neoproterozoic mantle superplume beneath Rodinia? Precambrian Res. 146, 1–15.
Li, Y.J., Song, W.J., Wu, G.Y., Wang, Y.F., Li, Y.P., Zheng, D.M., 2005. Jinning grano-diorite and diorite deeply concealed in the central Tarim Basin. Sci. in China (D-series) 48, 2061–2068.
Li, Y.J., Sun, L.D., Hu, S.L., Song, W.J., Wang, G.L., Tan, Z.J., 2003. 40Ar–39Ar geo-chronology of the granite and diorite revealed at the bottom of Tacan 1, the deepest well in China. Acta Petrol. Sin. 19, 530–536 (in Chinese with English abstract).
Ludwig, K.R., 2003. User's manual for Isoplot 3.00: a geochronological toolkit for Microsoft Excel. Kenneth R. Ludwig.
Ludwig, K.R., 2008. User's Manual for Isoplot 3.70: A Geochronological Toolkit for Microsoft Excel. Berkeley Geochronology Center Special Publication 477.
Lu, S.N., 1992. The Proterozoic tectonic evolution of Kuruketage, Xinjiang. J. Tianjin Geol. Min. Res. 26–27, 279–292 (in Chinese with English abstract).
Lu, S.N., Li, H.K., Zhang, C.L., Niu, G.H., 2008. Geological and geochronological evidence for the Precambrian evolution of the Tarim Block and surrounding continental fragments. Precambrian Res. 160, 94–107.
McCulloch, M.T., Gregory, R.T., Wasserburgm, G.J., Taylor Jr., H.P., 1981. Sm-Nd, Rb-Sr, and $^{18}O/^{16}O$ isotopic systematics in an oceanic crustal section: evidence from the Samail ophiolite. J. Geophys. Res. 86, 2721–2735.
Moabi, N.G., Grantham, G.H., Roberts, J., le Roux, P., 2017. The geology and geochem-istry of the Straumsnutane Formation, Straumsnutane, western Dronning Maud Land, Antarctica and its tectonic setting on the western margin of the Kalahari Craton: additional evidence linking it to the Umkondo Large Igneous Province. In: Pant, N.C., Dasgupta, S. (eds) 2017. Crustal Evolution of India and Antarctica: The Supercontinent Connection. Geological Society, London, Special Publications, 457, 61–85.
Nelson, D.R., 1997. Compilation of SHRIMP U-Pb zircon geochronology data, 1996, Geological Survey of Western Australia Record 1997/2: Perth. Geological Survey of Western Australia, Australia, pp. 189.
Pearce, J.A., Harris, N.B.W., Tindle, A.G., 1984. Trace element discrimination diagrams for the tectonic interpretation of granitic rocks. J. Petrol. 25, 956–983.
Pearce, J.A., 2008. Geochemical fingerprinting of oceanic basalts with applications to ophiolite classification and the search for Archean oceanic crust. Lithos 100, 14–48.
Pearce, J.A., 2014. Immobile element fingerprinting of ophiolites. Elements 10, 101–108.
Peng, P. (2010). Reconstruction and interpretation of giant mafic dyke swarms: a case study of 1.78 Ga magmatism in the North China craton. In: Kusky, T.M., Zhai, M.-G., & Xiao, W. (eds.), The Evolving Continents: Understanding Processes of Continental Growth. London: Geological Society of London, Special Publication 338, pp. 163–178.
Rogers, J.J.W., Santosh, M., 2002. Configuration of Columbia, a Mesoproterozoic Supercontinent. Gondwana Res. 5, 5–22.
Rogers, J.J.W., Santosh, M., 2009. Tectonics and surface effects of the supercontinent Columbia. Gondwana Res. 15, 373–380.
Salminen, J., Hanson, R., Evans, D.A.D., Gong, Z., Larson, T., Walker, O., Gumsley, A., Söderlund, U., Ernst, R., 2018. Direct Mesoproterozoic connection of Congo and Kalahari cratons in proto-Africa: Strange attractors across supercontinental cycles. Geology 46, 1011–1014.
Sylvester, P.J., 1989. Post-collisional alkaline granites. J. Geol. 261–280.
Sun, S.S., McDonough, W.F., 1989. Chemical and isotopic systematics of oceanic basalt: implication for mantle composition and processes. In: Saunders, A.D., Morry, M.J. (Eds.), Magmatism in the Ocean Basin. Geol. Soc. London Spec. Pub. 42, 528–548.
Teixeira, W., Hamilton, M.A., Girardi, V.A.V., Faleiros, F.M., Ernst, R.E., 2018. U-Pb baddeleyite ages of key dyke swarms in the Amazonian Craton (Carajás/Rio Maria and Rio Apa areas): tectonic implications for events at 1880, 1110 Ma, 535 Ma and 200 Ma. Precambrian Res in press.
Vermeesch, P., 2006. Tectonic discrimination diagrams revisited. Geochem. Geophys. Geosyst. 7, Q06017. https://doi.org/10.1029/2005GC001092.
Wang, C., Wang, Y.H., Liu, L., He, S.P., Li, R.S., Li, M., Yang, W.Q., Cao, Y.-T., Meert, J.G., Shi, C., 2014. The Paleoproterozoic magmatic–metamorphic events and cover sedi-ments of the Tiekelik Belt and their tectonic implications for the southern margin of the Tarim Block, northwestern China. Precambrian Res. 254, 210–225.
Wang, A.G., Zhang, C.L., Zhao, Y., Guo, K.Y., Dong, Y.G., 2004. Depositional types of the lower part of the Nanhua system at the northern margin of the SW Tarim and its tectonic significance. J. Strati. 28, 248–256 (in Chinese with English abstract).
Whalen, J.B., Currie, K.L., Chappell, B.W., 1987. A-type granites-geochemical char-acteristics, discrimination and petrogenesis. Cont. Mineral. Petrol. 95, 407–419.
Winchester, J.A., Floyd, P.A., 1977. Geochemical discrimination of different magma series and their differentiation products using immobile elements. Chem. Geol. 20, 325–343.
Wu, G.H., Chen, Z.Y., Qu, Y.L., Zhang, C.Z., 2012. SHRIMP zircon age of the high aero-magnetic anomaly zone in central Tarim Basin and its geological implications. Natural Sci. 4, 1–4.
Wu, G.H., Xiao, Y., Bonin, B., Ma, D.B., Li, X., Zhu, G.Y., 2018. Ca. 850 Ma magmatic events in the Tarim Block: age, geochemistry and implications for assembly of Rodinia supercontinent. Precambrian Res. 305, 489–503.
Workman, R.K., Hart, S.R., 2005. Major and trace element composition of the depleted MORB mantle (DMM). Earth Planet. Sci. Lett. 231 (1–2), 53–72.
Wu, F.Y., Yang, Y.H., Xie, L.W., Yang, J.H., Xu, P., 2006. Hf isotopic compositions of the standard zircons and baddeleyites used in U-Pb geochronology. Chem. Geol. 234, 105–126.
Zou, H.B., McKeegan, K.M., Xu, X.S., Zindler, A., 2004. Fe-Al-rich tridymite-hercynite xenoliths with positive cerium anomalies: preserved lateritic paleosols and implica-tions for Miocene climate. Chem. Geol. 207, 101–116.
Xinjiang, B.G.M.R., 1993. Regional Geology of the Xinjiang Uygur Autonomous Region. Geological Publishing House, Beijing, pp. 17–45.
Xu, B., Jiang, P., Zheng, H.F., Zou, H.B., Zhang, L.F., Liu, D.Y., 2005. U-Pb zircon geo-chronology of Neoproterozoic volcanic rocks in the Tarim Block of northwest China: implications for the breakup of Rodinia supercontinent and Neoproterozoic glacia-tions. Precambrian Res. 136, 107–123.
Xu, B., Xiao, S.H., Zou, H.B., Chen, Y., Li, Z.X., Song, B., Liu, D.Y., Zhou, C.M., Yuan, X.L., 2009. SHRIMP zircon U-Pb age constraints on Neoproterozoic Quruqtagh diamictites in NW China. Precambrian Res. 168, 247–258.
Xu, Z.Q., He, B.Z., Zhang, C.L., Zhang, J.X., Wang, Z.M., Cai, Z.H., 2013a. Tectonic frame-work and crustal evolution of the Precambrian basement of the Tarim Block inNW China: new geochronological evidence from deep drilling samples. Precambrian Res. 235, 150–162.
Xu, B., Zou, H.B., Chen, Y., He, J.Y., Wang, Y., 2013b. The Sugetbrak basalts from northwestern Tarim Block of northwest China: Geochronology, geochemistry and implications for Rodinia breakup and ice age in the Late Neoproterozoic. Precambrian Res. 236, 214–226.
Yang, H.J., Wu, G.H., Kusky, T.M., Chen, Y.Q., Xiao, Y., 2018. Paleoproterozoic assembly of the North and South Tarim terranes: new insights from deep seismic profiles and Precambrian granite cores. Precambrian Res. 305, 489–503.
Ye, X.T., Zhang, C.L., Santosh, M., Zhang, J., Fan, X.K., Zhang, J.J., 2016. Growth and evolution of Precambrian continental crust in the southwestern Tarim terrane: new evidence from the ca. 1.4 Ga A-type granites and Paleoproterozoic intrusive com-plexg. Precambrian Res. 275, 18–34.
Yin, A., Nie, S., 1996. A Phanerozoic palinspastic reconstruction of China and its neigh-boring regions. In: Yin, A., Harrison, T.M. (Eds.), The Tectonics of Asia: New York. Cambridge University Press, pp. 442–485.
Yong, W., Zhang, L., Hall, C., Mukasa, S., Essene, E., 2013. The $^{40}Ar/^{39}Ar$ and Rb–Sr chronology of the Precambrian Aksu blueschists in western China. J. Asi. Earth Sci. 63, 197–205.
Yuan, C., Sun, M., Yang, J.S., Zhou, H., Zhou, M.F., 2004. Nb-depleted, continental rift-related Akaz metavolcanic rocks (West Kunlun): implication for the rifting of the Tarim Block from Gondwana. Geo. Soc. London Speci. Pub. 226, 131–143.

Zilio, L.D., Faccenda, M., Capitanio, F., 2018. The role of deep subduction in supercontinent breakup. Tectonophysics. https://doi.org/10.1016/j.tecto.2017. 03.006.
Zhang, C.L., Dong, Y.G., Zhao, Y., 2003. Geochemistry of Meso-Proterozoic volcanites in Western Kunlun: evidence for the plate tectonic evolution. Acta Geol. Sinica 77, 237–245.
Zhang, C.L., Li, Z.X., Li, X.H., Ye, H.M., 2007. Early Palaeoproterozoic high-K intrusive complex in southwestern Tarim Block, NW China: age, geochemistry and implications for the Paleoproterozoic tectonic evolution of Tarim. Gondwana Rese. 12, 101–112.
Zhang, C.L., Yang, D.S., Wang, H.Y., 2010. Neoproterozoic mafic dyke swarm and basalt in southern margin of the Tarim Block: age, geochemistry and their geodynamic implications. Acta Geol. Sin. 84, 549–562.
Zhang, S.H., Li, Z.X., Evans, D.A., Wu, H.C., Li, H., Dong, J., 2012a. Pre-Rodinia supercontinent Nuna shaping up: A global synthesis with new paleomagnetic results from North China. Earth Planet. Sci. Lett. 353–354, 145–155.
Zhang, C.L., Zou, H.B., Li, H.K., Wang, H.Y., 2012b. Multiple phases of Neoproterozoic ultramafic-mafic complex in Kuruqtagh, northern margin of Tarim: interaction between plate subduction and mantle plume? Precambrian Res. 222–223, 488–502.
Zhang, C.L., Li, H.K., Santosh, M., Li, Z.X., Zou, H.B., Wang, H.Y., Ye, H.M., 2012c. Precambrian evolution and cratonization of the Tarim Block, NW China: Petrology, geochemistry, Nd-isotopes and U-Pb zircon geochronology from Archaean gabbro-TTG-potassic granite suite and Paleoproterozoic metamorphic belt. J. Asi. Earth Sci. 47, 5–20.
Zhang, C.L., Zou, H.B., Li, H.K., 2013. Tectonic framework and evolution of the Tarim Block, NW China. Gondwana Res. 23, 1306–1315.
Zhang, C.L., Zou, H.B., Santosh, M., Ye, X.T., Li, H.K., 2014a. Is the Precambrian basement of the Tarim Block in NW China composed of discrete terranes? Precambrian Res. 254, 226–244.
Zhang, J., Zhang, C.L., Li, H.K., Ye, X.T., Geng, J.X., Zhou, H.Y., 2014b. Revisit to time and tectonic environment of the Aksu blueschist terrane in northern Tarim, NW China: new evidence from zircon U-Pb age and Hf isotope. Acta Petrologica Sinica 30, 3357–3365.
Zhang, C.L., Ye, X.T., Zou, H.B., Chen, X.Y., 2016. Neoproterozoic sedimentary basin evolution in southwestern Tarim, NW China: new evidence from field observations, detrital zircon U-Pb ages and Hf isotope compositions. Precambrian Res. 280, 31–45.
Zhao, G.C., Cawood, P.A., Wilde, S.A., Sun, M., 2002. Review of global 2.1–1. 8Ga orogens: implications for a pre-Rodinia supercontinent. Earth-Sci. Rev. 59, 125–162.
Zhao, G.C., Li, S.Z., Sun, M., Wilde, S.A., 2011. Assembly, accretion, and break-up of the Palaeo-Mesoproterozoic Columbia supercontinent: records in the North China Craton revisited. Int. Geol. Rev. 53, 1331–1356.
Zhao, G.C., Cawood, P.A., 2012. Precambrian geology of the North China, South China and Tarim Blocks. Precambrian Res. 222–223, 13–54.
Zhan, S., Chen, Y., Xu, B., Wang, B., Faure, M., 2007. Late Neoproterozoic palaeomagnetic results from the Sugetbrak Formation of the Aksu area, Tarim basin (NW China) and their implications to paleogeographic reconstructions and the snowball Earth hypothesis. Precambrian Res. 154, 143–158.
Zheng, Y.F., Xiao, W.J., Zhao, G.C., 2013. Introduction to tectonics of China. Gondwana Res. 23, 1189–1206.
Zuza, A.V., Yin, A., 2017. Balkatach hypothesis: A new model for the evolution of the Pacific, Tethyan, and Paleo-Asian oceanic domains. Geosphere 13, 1664–1712.